Functional consequences of convergently evolved microscopic skin features on snake locomotion

Jennifer M. Rieser[a,b,1,2] , Tai-De Li[c,d,1], Jessica L. Tingle[e] , Daniel I. Goldman[b] , and Joseph R. Mendelson III[f,g]

[a]Department of Physics, Emory University, Atlanta, GA 30322; [b]School of Physics, Georgia Institute of Technology, Atlanta, GA 30332; [c]Advanced Science Research Center at Graduate Center, City University of New York, New York, NY 10031; [d]Department of Physics at City College of New York, City University of New York, New York, NY 10031; [e]Department of Evolution, Ecology, and Organismal Biology, University of California, Riverside, CA 92521; [f]School of Biological Sciences, Georgia Institute of Technology, Atlanta, GA 30332; and [g]Department of Research, Zoo Atlanta, Atlanta, GA 30315

The small structures that decorate biological surfaces can significantly affect behavior, yet the diversity of animal–environment interactions essential for survival makes ascribing functions to structures challenging. Microscopic skin textures may be particularly important for snakes and other limbless locomotors, where substrate interactions are mediated solely through body contact. While previous studies have characterized ventral surface features of some snake species, the functional consequences of these textures are not fully understood. Here, we perform a comparative study, combining atomic force microscopy measurements with mathematical modeling to generate predictions that link microscopic textures to locomotor performance. We discover an evolutionary convergence in the ventral skin structures of a few sidewinding specialist vipers that inhabit sandy deserts—an isotropic texture that is distinct from the head-to-tail-oriented, micrometer-sized spikes observed on a phylogenetically broad sampling of nonsidewinding vipers and other snakes from diverse habitats and wide geographic range. A mathematical model that relates structural directionality to frictional anisotropy reveals that isotropy enhances movement during sidewinding, whereas anisotropy improves movement during slithering via lateral undulation of the body. Our results highlight how an integrated approach can provide quantitative predictions for structure–function relationships and insights into behavioral and evolutionary adaptations in biological systems.

snake | locomotion | evolution | structure | function

Small surface features, ubiquitous in biological systems, can have profound and diverse functional consequences (1). While developing a link between microscopic structure and macroscopic function is challenging in general, some progress has been made in specific systems, where surface-characterization techniques are combined with mathematical or physical modeling. For example, nanostructured and microstructured patterns on biological surfaces manipulate interactions with light and can greatly affect appearance (2, 3); microscopic hair-like structures enhance adhesion (4) and manipulate fluid flows (5); microscopic denticles on shark skin affect fluid flows (6, 7); and microscopic cilia on bird feathers help to stabilize wing shape and improve flight mechanics (8). Here, we build upon the approach taken in these studies, combining surface-characterization techniques and mathematical modeling as a part of a comparative study across snake species from diverse habitats (Fig. 1) to develop an understanding of how putative evolutionary adaptations may affect snake locomotion.

Limbless locomotion is achieved through the use of properly coordinated sequences of body curvatures that push on the surrounding environment to generate propulsive forces—an interaction that in terrestrial situations is primarily mediated by the highly frictional interface between the body's ventral surface and the substrate. A common strategy for generating movement [and one that all snakes are capable of (11)] is lateral

undulation—in which an animal creates and subsequently propagates lateral body bends from head to tail, producing overall displacements primarily in the cranial direction. An example of this movement pattern in *Chionactis occipitalis* (Colubridae) (Fig. 2*A*), a desert specialist, is shown for two cycles of lateral undulation in Fig. 2*B*.

Some snakes have adopted modifications to this mode of movement, where a coupled, but independently modulated, vertical wave of body bending is also generated and propagated from head to tail. Depending on the environment and lifting pattern, this vertical wave can act to modulate environmental contact—leading to enhanced speed through drag reduction during typical slithering locomotion (12), improved maneuverability on sandy slopes through weight distribution modulations that help reduce avalanching events during sidewinding (13)—and has even been shown to stabilize the aerial glides of arboreal snakes (14). Here, we focus on the differences between sidewinding specialists and other vipers that primarily use other modes of locomotion.

During sidewinding, a 90° phase-shifted vertical traveling wave creates nearly static contact patches with the substrate that, when coupled to the lateral wave, enables the animal to move forward at an angle (relative to the cranial–caudal axis) in a continuing series of steps (13, 15) (Fig. 2 *D* and *E*). Specialization for sidewinding has evolved a small number of times and has been best characterized in the sidewinder rattlesnake (*Crotalus cerastes*), a pitviper from North American deserts, and in several true vipers (e.g., *Cerastes* species [spp.], *Pseudocerastes* spp., and *Bitis* spp.) from African and Middle Eastern deserts (16). Despite the unique mode of locomotion, the only

Significance

Animal skins are complex, highly specialized surfaces that are decorated with a variety of small structural features, whose functional benefits are often unknown. We investigate the microscopic features present on snake skins—which serve as the only interface between these animals and their environments—and we discover that distantly related sidewinding vipers have a unique structure that is distinct from other snakes. We develop a mathematical model that links structure to function and provides insight into evolutionary and behavioral adaptation in limbless locomotion.
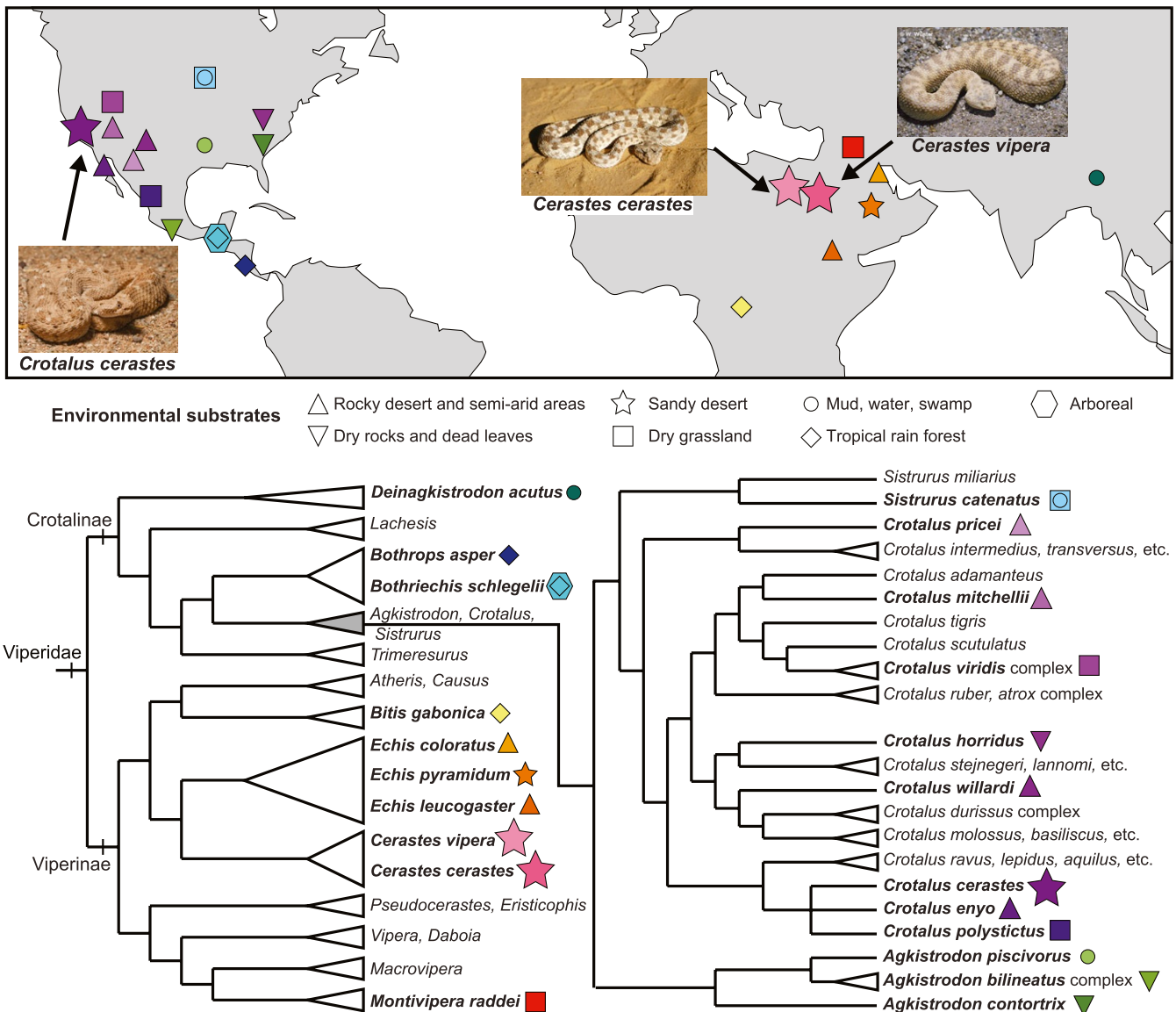
www.manaraa.com

Fig. 1. Geography and phylogeny of vipers. (*Upper*) World map showing approximate geographic locations of 22 viper species. Symbols indicate natural substrates, and colors distinguish species within a habitat. (*Lower*) Phylogeny of viperid snakes (data from ref. 9), with the pitviper (Crotalinae) clade expanded to the right (data from refs. 9 and 10). we show a conservative polytomy for the topology of the subclade (*Cr. cerastes*, *Cr. enyo*, and *Cr. polystictus*). Bold text and colored symbols (consistent with map labels) identify species investigated here. Cladistic and geographic patterns underscore the independent, convergent nature of sidewinding locomotion (bolded stars) in the American sidewinder (*Cr. cerastes*), a crotaline pitviper, and the African sidewinding viperine vipers (*Cerastes* spp.). Each snake shown is approximately 35 cm in length. *Cr. Cerastes* and *Ce. Vipera* images credit: Wolfgang Wuster (photographer). *Ce. cerastes* image credit: iStock/acceptfoto. Map image credit: VectorStock/SpicyTruffel.

morphologically distinctive feature identified thus far is a shorter musculus semispinalis-spinalis, a muscle likely involved in lifting portions of a snake's body (17, 18).

Atomic force microscopy (AFM) surface characterization of the ventral scales from shed skins of *Ch. occipitalis* (Fig. 2C) revealed a structurally anisotropic texture in which the epidermal skin cells have caudally directed, elevated, regular, micrometer-sized spikes we refer to as *microspicules*; previous literature has inconsistently used other terms for these structures (e.g., microfibrils, denticles, or digits) that we feel offer poor or misleading anatomical characterizations (19–21). The anatomy seen in *Ch. occipitalis* is qualitatively similar to those found in previous studies of many nonviperid alethinophidian snakes (19, 20, 22–30). This configuration of the microspicules produces longitudinal structural anisotropy on the ventral surface that is closely associated with lateral undulation and with other types of cra-

nially oriented movement. In contrast, we found that *Cr. cerastes* possessed a different, more isotropic texture with greatly reduced microspicules and large impressions; similar, but smaller, structures in other species that have been referred to as pits or holes (21) (Fig. 2F). To investigate whether these differences in textures relate to movement patterns or details of the environmental interactions, we characterized the microscopic textures on the ventral scales of a broad range of species within the viper family (7 Viperinae and 15 Crotalinae). Fig. 3 A and B, *Left* show 10 μm × 10 μm regions on three nonsidewinding species and three sidewinding species. We observed qualitatively similar textures in the nonsidewinding crotalines (pitvipers), comprising regularly arranged, elongated, sharply pointed, caudally protruding microspicules oriented along the longitudinal axis of the body; we consider this to be the ancestral (plesiomorphic) morphology for the clade (Fig. 3A). The main differences in textures
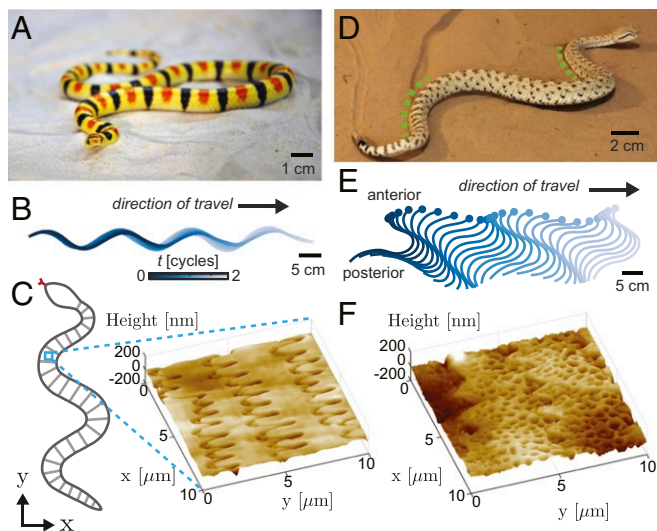
Fig. 2. Undulatory locomotion modes of two sand-specialist snakes. (*A*) The shovel-nosed snake (Colubridae: *Ch. occipitalis*). Reprinted from ref. 46. (*B*) Time trace of splined points along the body as the snake moves on 300-μm glass beads via lateral undulation. (*C*, *Left*) Schematic of the underside of a snake; transverse lines represent ventral scales with the blue box highlighting that our scan regions are subscale in size (not to scale). (*C*, *Right*) AFM scan of microscopic structure within one ventral scale of *Ch. occipitalis*. (*D*) The sidewinder (Viperidae: *Cr. cerastes*). Green dashed lines indicate regions of body–substrate contact. (*E*) Time trace of splined points along the body as the snake sidewinds on natural sand. (*F*) AFM scan of microscopic structure within one ventral scale of *Cr. cerastes*. We note that the posterior–anterior axis in *C* and *F* is aligned with the *y* axis, and larger *y* values are closer to the head of the animal.

across species are quantitative, primarily intramicrospicule and intermicrospicule length variations (Fig. 3*A* and *SI Appendix*, Table S1). In contrast, *Cr. cerastes* (Fig. 3 *B*, *Upper Left*) has a remarkably different (derived) morphology—greatly reduced microspicules and the presence of isotropic pits—that is distinct from close relatives *Crotalus polystictus* (Fig. 3*A*, *Upper Left*) and *Crotalus enyo* (*SI Appendix*, Fig. S1 and Table S1).

Our smaller sampling of Viperinae (true vipers) also revealed a general pattern of caudally projecting microspicules, but with more variability in size and shape across species than is evident in pitvipers (*SI Appendix*, Figs. S1 and S2 and Table S1). While the ancestral morphology of the viperine clade is not clear from our sampling, we find that the North African sidewinding vipers, *Cerastes cerastes* and *Cerastes vipera*, have distinct textures—marked by the absence of microspicules and the presence of isotropic pits—that are morphologically similar to that of the American sidewinder, *Cr. cerastes* (Fig. 3*B*).

The convergent evolution of similar isotropic textures in the North American sidewinder rattlesnake (*Cr. cerastes*) and in distantly related North African sidewinding specialists (*Cerastes* spp.) under similar environmental conditions suggests adaptation. Moreover, the fact that a laterally undulating sand specialist (*Ch. occipitalis*) retains an anisotropic condition (Fig. 2*C*) suggests that isotropy is related specifically to sidewinding locomotion, rather than to sandy habitats. The species that use sidewinding as their primary mode of locomotion differ in the degree to which they show derived morphology: North American *Cr. cerastes* have greatly reduced microspicules and enlarged, cratered, epidermal pits, whereas in North African *Cerastes* spp., the microspicules are completely absent, and the enlarged epidermal pits are more smoothly bounded than in the American sidewinder. That the North American species appears somewhat less morphologically specialized is consistent with the context of Earth's geologic history and viperid evolutionary history. Fos-

sil dunes indicate that sandy desert conditions appeared in the Sahara region at least 7 million years ago, and the geologic record shows that arid conditions have cyclically prevailed since (31, 32). In contrast, the Mojave Desert of North America first accumulated sand only about 15,000 to 20,000 years ago (33, 34). Additionally, an ancestral state reconstruction shows that the common ancestor of North African *Cerastes* spp. had most likely evolved specialization for sidewinding by about 16 million years ago, while the most recent common ancestor of North American sidewinders and their sister species (about 11 million years ago) probably did not sidewind (16).

In addition to the three sidewinding specialists, *Echis pyramidum* sidewinds regularly and proficiently on sand, but uses other types of locomotion on nonsand substrates, while *Echis coloratus* can sidewind when frightened or when placed on shifting or smooth substrates, though it lives in rocky habitats (35–37). The ventral surface of *E. pyramidum* lacks microspicules and has a low structural anisotropy (*SI Appendix*, Fig. S1). The ventral surface of *E. coloratus* does not resemble that of the specialized sidewinders.

Although we were unable to obtain samples for sidewinding species in other genera, we can make predictions as to their degree of morphological specialization. *Pseudocerastes* spp. and *Eristicophis macmahoni* should possess highly specialized scale morphology, similar to *Cerastes* spp., considering that their shared ancestor about 21 million years ago was likely a specialized sidewinder (16). Sidewinding specialization in an ancestor of *Bitis peringueyi* and *Bitis caudalis* may have evolved more recently, perhaps only 6 million or 7 million years ago (16). Their ventral scales may therefore show only partial loss of the anisotropic condition, similar to *Cr. cerastes*. *Echis carinatus* may similarly show incomplete specialization in scale microtexture. If future studies confirm our predictions, the results would indicate
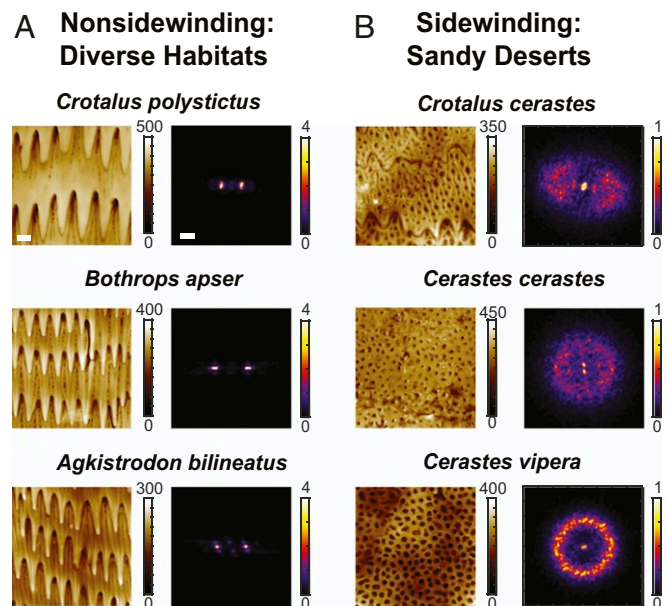

Fig. 3. Microscopic ventral scale structures. AFM scans were performed to examine the structure of a subsample of a single scale (as illustrated by the light blue box in the schematic of Fig. 2*C*). Three 10-μm × 10-μm scans (color indicates height in nanometers) and their corresponding 2D power spectra are shown for three representative nonsidewinding species (*A*) and three sidewinding species (*B*). All scans are oriented such that the head (tail) is toward the top (bottom) of the page. The bright spots in the power spectra for nonsidewinding species confirm the presence of a strong structural anisotropy oriented along the body across species and environments. For all sidewinding species scanned, the power spectra are more isotropic, indicating a lack of (or reduced) structural anisotropy.

EVOLUTION

BIOPHYSICS AND COMPUTATIONAL BIOLOGY

that the evolution of sidewinding behavior likely preceded the evolution of highly specialized scale morphology.

We quantitatively compared microtextures by computing the two-dimensional (2D) power spectrum of a 20-μm × 20-μm AFM scan region for each species (Fig. 3 *A* and *B*, *Right*; *SI Appendix*, Fig. S1). Sharp peaks in the power spectra result from periodic structures, with peak locations identifying both dominant feature lengths and corresponding directions of periodicity. For the nonsidewinding species investigated, the strongest peaks are oriented along the horizontal axis, indicating that the lateral structure is the dominant feature in the array of microspicules. In contrast, the structures of the three sidewinding species sampled lack a strong direction dependence, as indicated by the nearly radially symmetric appearance of the power spectra in Fig. 3*B*. To quantify the observed differences in the textures, we created a structural anisotropy index, s, that compares the angular variation in the power spectra along the dominant structural direction and the orthogonal direction.

To determine s, we computed the radon transform of each power spectrum and defined the dominant structural direction by the brightest pixel value; s was then defined as the Jensen–Shannon divergence (38) of two slices through the radon transform: the one along the dominant direction and the one orthogonal to the dominant direction (Fig. 4 *A* and *B*). The three sidewinding specialists investigated here all have low values of s ($s < 0.1$) and are among the lowest values of all vipers sampled, indicating that the microtextures are more isotropic than most species we investigated. We note that s is bounded between zero and one, with zero indicating the two directions have identical features and one indicating maximal dissimilarity (see *Materials and Methods* for details). The relative isotropy of the evidently nonsidewinding viperine *Montivipera raddei* (Fig. 4*C*) is an interesting result and suggests that microstructural evolution in the viperine clade is worthy of subsequent investigation. Low anisotropy in the pitviper *Agkistrodon piscivorus* may be associated with relaxed selection for anisotropy due to its semi-aquatic habits and/or use of muddy substrates, and this also invites further investigation.

Previous AFM investigations of the structurally anisotropic microspicule textures have measured a drag-direction-dependent microscopic friction coefficient, with smaller values for forward movement (from head to tail) along the body (19, 23, 26–30, 39). Larger friction coefficients have consistently been reported for backward (tail to head) movement, and, while there has been some sensitivity to experimental details, some studies have reported similarly large friction coefficients for lateral movement across the body in both natural and artificial microspicule structures (23, 26–29). Previously reported macroscopic measurements of friction are qualitatively consistent with microscopic measurements, reporting a larger value for backward movement relative to forward movement (12, 40) and a larger value for lateral movement relative to forward movement (12). However, thus far, hypotheses about the mechanical importance of these textures for locomotion have focused on the forward/backward anisotropy.

Like previous researchers, we expect that the direction-dependent friction coefficient results from the structural anisotropy. However, given the dominance of the lateral features, as indicated by the power spectra in Fig. 3*A* (and *SI Appendix*, Fig. S1), we hypothesized that the lateral/forward anisotropy is important particularly for lateral undulation, which is common for snakes with these anisotropic structures. We developed a mathematical model of a snake and used a modified granular resistive force theory (RFT) (41–43) to model environmental interactions and systematically probe how frictional anisotropy affects locomotion (*Materials and Methods*). To decouple the anisotropy associated with flowable substrates (e.g., s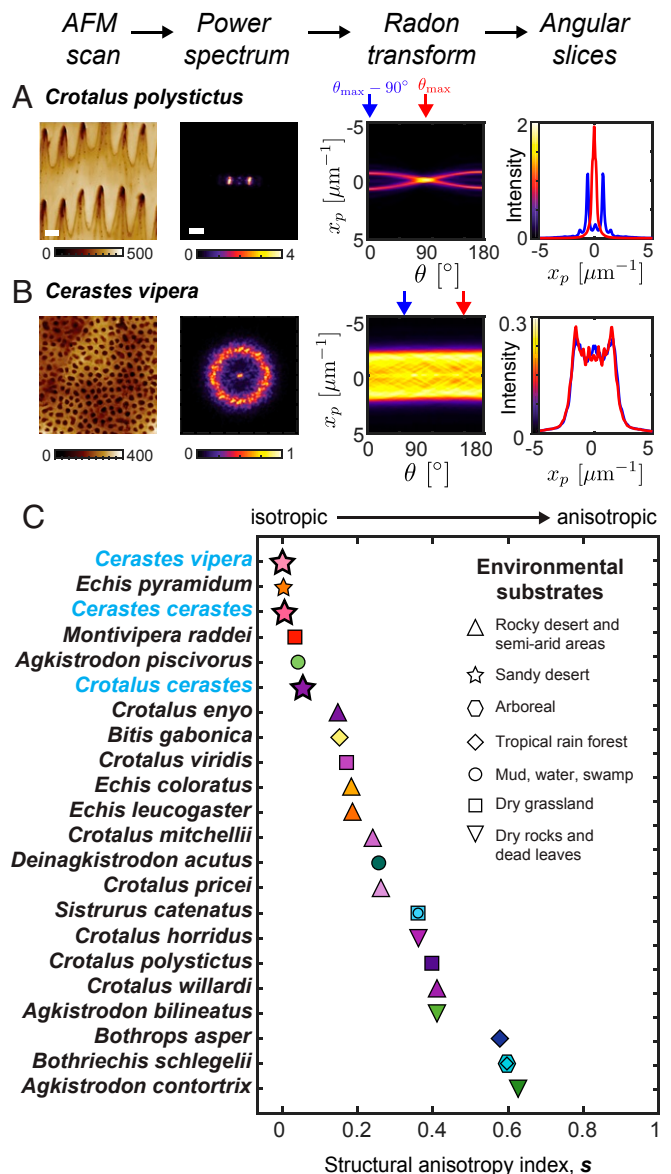ee ref. 44) from the hypothesized contribution of microstructural features present on the body, we modeled the substrate interactions with kinetic Coulomb friction (45).

Our hypothesized relationship between structure and friction is shown in Fig. 5*A*; arrows in the enlarged regions to the right identify directions associated with lower friction. We define a frictional anisotropy coefficient, c, as the ratio of the lateral (locally transverse to the body midline) to longitudinal friction coefficients (locally aligned with the body midline). If $c = 1$ (i.e., standard kinetic Coulomb friction), then movement along all directions results in the same frictional force. If $c > 1$, the transverse friction is larger than the longitudinal friction. If $c < 1$, then transverse friction would be lower than longitudinal friction, though, to our knowledge, this condition has not

Fig. 4. Quantification of structural anisotropy. We define a structural anisotropy index, *s*, by taking the radon transform of the power spectrum and comparing the radial profiles of the radon transform along the dominant angular direction, θ_{max}, and the orthogonal direction, $\theta_{max} - 90°$. (*A* and *B*) These steps are shown for *Cr. polystictus* (*A*) and *Ce. vipera* (*B*). (*C*) The Jensen–Shannon divergence of the two radon profiles provides a quantification of the structural anisotropy (see *Materials and Methods* for details). The three sidewinding specialists investigated here (labeled with blue text) have nearly isotropic microtextures.
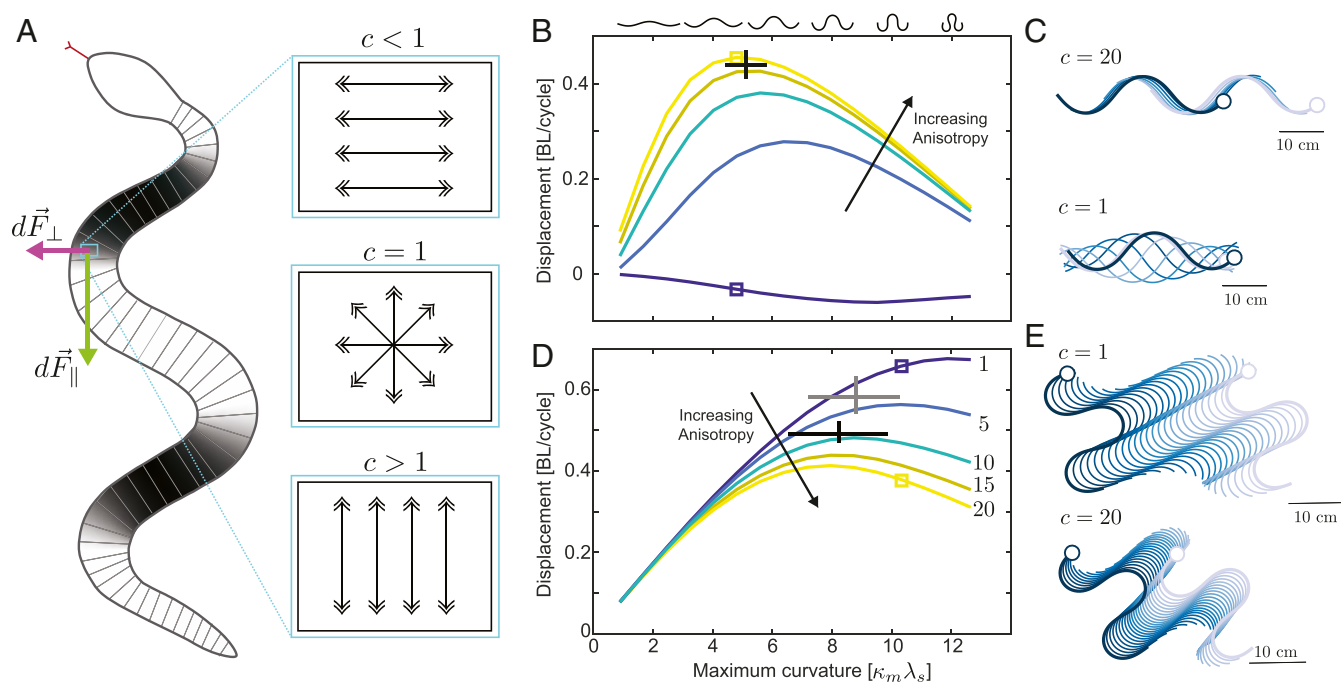
www.manaraa.com

Fig. 5. Performance varies with anisotropy. (*A*) Schematic of the model. The body is divided into small segments, each of which experiences an environmental force, with components both parallel and perpendicular to the long axis of the body. Arrow sketches in *A, Right* show a hypothesized connection between microspicule structure and relative ease of movement, where arrows indicate the direction associated with the smallest friction coefficient. For lateral undulation, all parts of the body are in contact with the ground. In sidewinding, the contact pattern changes throughout a gait cycle (13, 15) with sections of body alternately in contact with (black areas on snake schematic), or lifted above (white areas) the substrate. (*B*) Model-predicted displacements (in body lengths [BL] per undulation cycle) for lateral undulation as a function of maximum body curvature. Curves of different colors show predictions for different anisotropy values. (*C*) Model-generated kinematics for one cycle of movement for lateral undulation for c = 20 (*Upper*) and c = 1 (*Lower*). Curvatures and predicted displacements are highlighted by the square points in *B*. (*D*) Model-predicted displacements (BL/cycle) for sidewinding as a function of maximum body curvature, with color indicating anisotropy value. (*E*) Model-generated kinematics for one cycle of movement via sidewinding for c = 1 (*Upper*) and c = 20 (*Lower*). Curvatures and predicted displacements are highlighted by the square points in *D*.

been experimentally observed in snakes. We note that, as with other implementations of RFT, there is no forward (head to tail)/backward (tail to head) frictional anisotropy in our model.

For lateral undulation, all body segments were modeled to maintain substrate contact throughout movement; therefore, all segments were treated equally and experienced nonzero environmental reaction forces. Fig. 5*B* shows predicted displacements as a function of maximal nondimensional body curvature, $\kappa_m \lambda_s$, for a snake with $n = 1.5$ waves along the body (see *Materials and Methods* for more detail). For each curvature investigated, we found that lateral undulation performance was enhanced by higher c values. While we do not know the relationship between the microscopic structure and overall frictional anisotropy (or how substrate anisotropy may contribute to the overall frictional anisotropy), the experimentally measured performance of *Ch. occipitalis* moving on sand (the black cross in Fig. 5*B*; originally reported in refs. 44 and 45) is bounded by model predictions for high anisotropy values ($10 \leq c \leq 20$), and the range of observed curvature values nearly coincide with model-predicted peak performance per cycle. Examination of model-generated trajectories with curvature values within the range typically used by *Ch. occipitalis* (Fig. 2 *A* and *B*; refs. 44 and 46) reveals that when anisotropy is high ($c = 20$), the snake is predicted to move forward about 0.5 body lengths over the course of one undulation cycle (Fig. 5 *C, Upper*). However, when $c = 1$, nonzero locally transverse velocity components cause lateral (sideways) slip that hinders locomotion and prevents forward displacement (Fig. 5 *C, Lower*).

To adapt our model for sidewinding, we introduced a smoothly varying posture-dependent contact function (ranging from zero to one) that is consistent with previous characterizations of substrate contact in *Cr. cerastes* (13, 15, 45). This contact function

multiplies the forces of each infinitesimal segment and specifies how much each segment experiences substrate forces (with zero corresponding to fully lifted and one corresponding to full-contacted segments, respectively; see ref. 45 and *Materials and Methods* for more detail). The grayscale coloration of the snake schematic in Fig. 5*A* shows the prescribed contact pattern associated with this posture, with black regions on the ground and white regions fully lifted.

Predicted displacements for sidewinding are shown in Fig. 5*D* as a function of maximal body curvature for locomotors with $n = 1.5$ waves along the body. We note that all aspects of the model, aside from the variable contact pattern, are the same as the lateral undulation model. We predict enhanced performance for each curvature as anisotropy is decreased (i.e., for smaller values of c; Fig. 5*D*). Previously reported animal performance on both sand and smooth wood (Fig. 5*D*, black and gray crosses, respectively) revealed that animals displace further when moving on rigid substrates (bounded by model predictions for $1 \leq c \leq 5$), despite using similar curvatures on both hard and soft substrates (45); we attributed this difference in performance to an additional contribution to the overall frictional anisotropy arising from the flowable sand substrate. Examination of model-generated trajectories associated with curvature values used by the American sidewinder [*Cr. cerastes* (15, 45)] revealed that high anisotropy ($c > 1$) prevents slipping locally perpendicular to the body midline and, therefore, induces a velocity component along the midline and directed toward the tail (i.e., a backward slip) that opposes the overall direction of motion to achieve force balance. This backward slip hinders forward progress by decreasing the net displacement possible over the course of a cycle (Fig. 5 *E, Lower*). However, when there is no anisotropy ($c = 1$), the force

www.manaraa.com

balance produces a velocity component orthogonal to the overall direction of motion (i.e., a sideways slip) that does not oppose forward progress and, therefore, results in larger displacements over the course of an undulation cycle (Fig. 5 *E*, *Upper*).

Our modeling results reveal that a high lateral/longitudinal frictional anisotropy improves predicted forward displacements during lateral undulation, which we propose is provided (at least in part) by the periodic array of caudally projected microspicules observed on the ventral surfaces of laterally undulating snakes. This hypothesis is consistent with previous microscopic and macroscopic ventral friction measurements (12, 19, 23, 26–29, 39, 40). Our model-predicted displacements are in agreement with biological observations (13, 15, 44, 45), despite having excluded the backward/forward anisotropy that has been the focus of previous AFM studies. Our results, along with the quantitative agreement achieved by other RFT models (40–42, 45) (none of which include a backward/forward anisotropy), suggest that the lateral/longitudinal anisotropy is more important for undulatory locomotion than backward/forward anisotropy. Our model predicts that higher values of lateral/longitudinal anisotropy lead to enhanced performance for lateral undulation, which we posit is a consequence of the anisotropic microstructure. RFT modeling of sidewinding reveals that, unlike lateral undulation, performance enhanced by the lack of a lateral/longitudinal anisotropy. Previously reported biological sidewinding performance is in quantitative agreement with predictions for isotropic friction, which we hypothesize results from the observed isotropic ventral microstructure.

In this paper, we examined the microtextures present on the ventral surface of shed viper skins. In most snakes investigated, we found variations of a longitudinally oriented, caudally projecting, periodic array of microspicules. Surprisingly, we found two independent origins of a derived, nearly isotropic, pitted ventral microtexture in three viper species (Fig. 3*B*) that coincide with specialization for sidewinding locomotion, suggesting adaptation. These results provide a prediction for expected structural features on other sidewinding specialists that we did not have access to for this study. Though we do not yet have a precise quantitative mapping from structural anisotropy to friction, we created a model in which frictional anisotropy can be systematically varied. Our model revealed that anisotropic frictional interactions are beneficial for lateral undulation, but detrimental for sidewinding, suggesting that the nearly isotropic microtextures observed on sidewinders may enhance their locomotor performance. Previous work investigating the direction-dependent nature of nonsidewinding microtextures found a larger anisotropy when skin samples were mounted with soft backing (27), suggesting that frictional properties may be enhanced by the compliant soft tissues under the skin. It would be interesting to explore the potential dependence of the skin friction on the mechanical properties of underlying substrate, as well as the degree to which muscle-activation patterns may be able to control frictional interactions through modulations of microspicule protrusion. Previous studies have also noted the presence of external lipid layers on the ventral scales of least some snake species (47)—it would be interesting to explore the potential benefits of surface coatings (e.g., lubrication, traction, and/or wear mitigation) and how they may affect environmental interactions and frictional anisotropy. Finally, while other modes of limbless locomotion were outside the scope of this study, our approach could be used to explore other potential relationships and functional benefits of microstructures for other locomotor modes and, more broadly, other animal behaviors that are essential for survival.

Materials and Methods

Surface Characterization. Surface-topography images of skins were acquired by an AFM (Bruker Multimode 8) with a silicon nitride tip (Bruker Scanasyst-Air) under peak-force tapping mode in air. Samples with adherent dust (*Ce. cerastes* and *Ce. vipera*) were cleaned for 30 min by ultrasonicating in detergent (5% Cole-Parmer micro-90 in water). Water-rinsed and air-dried samples were then mounted on a glass substrate. No change was observed for the surface topography of a noncontaminated sample from *Crotalus viridis* before and after the cleaning treatment, demonstrating that the cleaning protocol did not alter the intrinsic surface.

We note that our study was not designed to examine variation in microstructure with regard to ontogeny or anatomical position, nor among individuals (reviewed by refs. 20, 26, and 48). Samples from a central point of midbody unwrinkled ventral scales from naturally shed skins of adult snakes were mounted for AFM analyses (per ref. 20, figure 13a). Qualitative and quantitative measures and terms used are consistent with ref. 21, however, choosing the term "microspicules" rather than the terms "digits," "microfibrils," or "denticles" used in some previous works. The impressions variously referred to as "pits" or "holes" (21) are common features in many snakes, but their function and homology are unclear (21, 22).

Data Analysis. To identify dominant structural features present in each AFM scan, we computed the power spectrum from a 20-μm $\times$ 20-μm region. Scan images were rescaled and converted to 8-bit unsigned integer images in Matlab, and then background variation was removed by using a contrast-limited adaptive histogram equalizer function (adapthisteq, with the image divided into 25 equally sized regions). The 2D power spectra were computed after each image was converted to a double-precision array, and the overall average was subtracted from the image. Each power spectrum was smoothed by using a 2D Gaussian filter (with $\sigma = 1$). All power spectra are shown in *SI Appendix*, Fig. S1.

We computed the radon transforms (*SI Appendix*, Fig. S3) to quantify the angular dependencies of the of each 2D power spectrum. We identified θ_{max}, the angle associated with the brightest pixel in each radon transform, and took vertical slices through the radon transform at θ_{max} and mod($\theta_{max} + \pi/2, \pi$). We compared these two slices through the radon transform using the Jensen–Shannon divergence (38), a measure of the distinguishability of two distributions that is bounded between zero (indistinguishable) and one (perfectly distinguishable) (*SI Appendix*, Fig. S3).

Modeling. RFT assumes that forces along a deforming body are decoupled, and, therefore, a locomotor can be divided into many infinitesimal segments that can be treated independently. Further, in dissipation-dominated environments, where inertial forces are negligible, the net force on a body is zero at every moment in time, yielding

$$\vec{\mathbf{F}}_{total} = \int (d\vec{\mathbf{F}}_{\parallel} + d\vec{\mathbf{F}}_{\perp}) = 0. \qquad [1]$$

Here, $d\vec{\mathbf{F}}_{\parallel}$ and $d\vec{\mathbf{F}}_{\perp}$ are the tangential and normal components, respectively, of the environmental force acting on an infinitesimal segment of the body (sketch in Fig. 5*A*).

$$d\vec{\mathbf{F}}_{\parallel} = -\mu_k mg(\hat{\mathbf{v}} \cdot \hat{\mathbf{t}})\hat{\mathbf{t}}, \qquad [2]$$
$$d\vec{\mathbf{F}}_{\perp} = -c\mu_k mg(\hat{\mathbf{v}} \cdot \hat{\mathbf{n}})\hat{\mathbf{n}}, \qquad [3]$$

where μ_k is the coefficient of kinetic friction, m is the mass of the segment, $g = 9.81$ m/s^2, and $\hat{\mathbf{t}}$ and $\hat{\mathbf{n}}$ are unit vectors locally tangent and normal to the body, respectively. We introduced and varied c, an anisotropy factor, to explore how the predicted performance depends on the magnitude of the normal forces relative to the tangential forces.

Snake Geometry. To parameterize the time-varying shape of the snake, we linked 100 small segments together end-to-end. Connections between segments were treated as position-controlled lateral joints, with angle $\zeta_i(t)$ at position i prescribed to vary sinusoidally along the body and through time, t, creating a serpenoid curve (49):

$$\zeta_i(t) = w_1(t) \sin(2\pi ni/N) + w_2(t) \cos(2\pi ni/N), \qquad [4]$$

where n is the number of waves along the body, $N = 100$ is the total number of segments along the body, and $w_1(t) = W \sin(2\pi ft)$ and $w_2(t) = W \cos(2\pi ft)$ are the time-varying angle amplitudes that produce a traveling wave propagated from head to tail, with temporal frequency f and amplitude W.

We note that animal-curvature values from previous studies were reported in terms $\kappa_m \lambda_s$, a nondimensional quantity originally defined in

www.manaraa.com

ref. 40. κ is the local curvature along the body, κ_m is the maximal value of κ, and λ_s is the arc-length of one wave. To relate $\kappa\lambda_s$ to joint angles, ζ_i, we note that λ_s is equal to L/n, the total body length divided by the number of waves along the body. κ_i is given by $\Delta\theta_i/\Delta s$, where Δs is the length of a single body segment (given by L/N), $\theta_i = \arctan(\Delta y_i/\Delta x_i)$ is the local tangent angle along the body, and $\Delta\theta_i$ is equivalent to ζ_i. Given these relations, $\kappa_i\lambda_s$ reduces to $\zeta_i N/n$, and $\kappa_m\lambda_s$ is equal to the maximum value of $\zeta_i N/n$.

Changing Contact. Previous work (15) revealed that the three-dimensional pose of *Cr. cerastes* could be represented by a horizontal wave coupled to a phase-shifted vertical wave that sets the environmental contact condition. To properly couple the vertical wave to the in-plane shape, we introduced $\delta(r)$

$$\delta(r) = \sin\left[\frac{2\pi n r}{L} + \tan^{-1}\left(\frac{w_2}{w_1}\right) - \frac{\pi}{2}\right], \quad [5]$$

where r is the position along the body, n is the number of waves on the body, L is the total length of the body, and w_1 and w_2 describe the in-plane wave shape. To set the contact using the vertical wave description, δ, we defined the smoothly varying function, S

$$S(\delta(r)) = \frac{1}{\exp[a\delta(r) + b]}. \quad [6]$$

Here, $S \in [0, 1]$ sets the local fraction of the environmental force experienced as a function of position, r, along the body, a sets contact width, and b sets the sharpness of the on/off ground transition along the body.

To be consistent with previous observations of *Cr. cerastes*, $a = 15$ and $b = 0.5$ were chosen so that, when averaged over a completed gait cycle, approximately 34% of the animal's body is on the ground (13).

Data Availability. Matlab files data have been deposited in the Open Science Framework (https://doi.org/10.17605/OSF.IO/KJ9TV; ref. 50).

1. S. N. Gorb, *Functional Surfaces in Biology: Little Structures with Big Effects* (Springer Science & Business Media, Dordrecht, Netherlands, 2009), vol. 1.
2. P. Vukusic, J. R. Sambles, Photonic structures in biology. *Nature* **424**, 852–855 (2003).
3. V. Sharma, M. Crne, J. O. Park, M. Srinivasarao, Structural origin of circularly polarized iridescence in jeweled beetles. *Science* **325**, 449–451 (2009).
4. K. Autumn, A. M. Peattie, Mechanisms of adhesion in geckos. *Integr. Comp. Biol.* **42**, 1081–1090 (2002).
5. A. Nasto, P. T. Brun, A. Hosoi, Viscous entrainment on hairy surfaces. *Phys. Rev. Fluids* **3**, 024002 (2018).
6. J. Oeffner, G. V. Lauder, The hydrodynamic function of shark skin and two biomimetic applications. *J. Exp. Biol.* **215**, 785–795 (2012).
7. G. V. Lauder *et al.*, Structure, biomimetics, and fluid dynamics of fish skin surfaces. *Phys. Rev. Fluids* **1**, 060502 (2016).
8. L. Y. Matloff *et al.*, How flight feathers stick together to form a continuous morphing wing. *Science* **367**, 293–297 (2020).
9. L. R. Alencar *et al.*, Diversification in vipers: Phylogenetic relationships, time of divergence and shifts in speciation rates. *Mol. Phylogenet. Evol.* **105**, 50–62 (2016).
10. J. Reyes-Velasco, J. M. Meik, E. N. Smith, T. A. Castoe, Phylogenetic relationships of the enigmatic longtailed rattlesnakes (*Crotalus ericsmithi*, *C. lannomi*, and *C. stejnegeri*). *Mol. Phylogenet. Evol.* **69**, 524–534 (2013).
11. H. B. Lillywhite, *How Snakes Work: Structure, Function and Behavior of the World's Snakes* (Oxford University Press, Oxford, UK, 2014).
12. D. L. Hu, J. Nirody, T. Scott, M. J. Shelley, The mechanics of slithering locomotion. *Proc. Natl. Acad. Sci. U.S.A.* **106**, 10081–10085 (2009).
13. H. Marvi *et al.*, Sidewinding with minimal slip: Snake and robot ascent of sandy slopes. *Science* **346**, 224–229 (2014).
14. I. J. Yeaton, S. D. Ross, G. A. Baumgardner, J. J. Socha, Undulation enables gliding in flying snakes. *Nat. Phys.* **16**, 974–982 (2020).
15. H. C. Astley *et al.*, Modulation of orthogonal body waves enables high maneuverability in sidewinding locomotion. *Proc. Natl. Acad. Sci. U.S.A.* **112**, 6200–6205 (2015).
16. J. L. Tingle, Facultatively sidewinding snakes and the origins of locomotor specialization. *Integr. Comp. Biol.* **60**, 202–214 (2020).
17. B. C. Jayne, Comparative morphology of the semispinalis-spinalis muscle of snakes and correlations with locomotion and constriction. *J. Morphol.* **172**, 83–96 (1982).
18. J. Tingle, G. Gartner, B. Jayne, T. Garland, Jr, Ecological and phylogenetic variability in the spinalis muscle of snakes. *J. Evol. Biol.* **30**, 2031–2043 (2017).
19. J. Hazel, M. Stone, M. Grace, V. Tsukruk, Nanoscale design of snake skin for reptation locomotions via friction anisotropy. *J. Biomech.* **32**, 477–484 (1999).
20. C. V. Schmidt, S. N. Gorb, Snake scale microstructure: Phylogenetic significance and functional adaptations. *Zoologica* **157**, 1–106 (2012).
21. M. I. Arrigo *et al.*, Phylogenetic mapping of scale nanostructure diversity in snakes. *BMC Evol. Biol.* **19**, 91 (2019).
22. D. J. Gower, Scale microornamentation of uropeltid snakes. *J. Morphol.* **258**, 249–268 (2003).
23. M. J. Benz, A. E. Kovalev, S. N. Gorb, "Anisotropic frictional properties in snakes" in *Bioinspiration, Biomimetics, and Bioreplication 2012*, A. Lakhtakia, Ed. (International Society for Optics and Photonics, SPIE, 2012), pp. 256–261.
24. H. Abdel-Aal, R. Vargiolu, H. Zahouani, M. El Mansori, Preliminary investigation of the frictional response of reptilian shed skin. *Wear* **290**, 51–60 (2012).
25. H. A. Abdel-Aal, M. El Mansori, Tribological analysis of the ventral scale structure in a python regius in relation to laser textured surfaces. *Surf. Topogr. Metrol. Prop.* **1**, 015001 (2013).
26. R. Berthé, G. Westhoff, H. Bleckmann, S. Gorb, Surface structure and frictional properties of the skin of the Amazon tree boa *Corallus hortulanus* (Squamata, Boidae). *J. Comp. Physiol.* **195**, 311–318 (2009).
27. M. J. Baum, A. E. Kovalev, J. Michels, S. N. Gorb, Anisotropic friction of the ventral scales in the snake *Lampropeltis getula californiae*. *Tribol. Lett.* **54**, 139–150 (2014).
28. M. J. Baum, L. Heepe, S. N. Gorb, Friction behavior of a microstructured polymer surface inspired by snake skin. *Beilstein J. Nanotechnol.* **5**, 83–97 (2014).
29. M. J. Baum, L. Heepe, E. Fadeeva, S. N. Gorb, Dry friction of microstructured polymer surfaces inspired by snake skin. *Beilstein J. Nanotechnol.* **5**, 1091–1103 (2014).
30. W. Wu *et al.*, Variation of the frictional anisotropy on ventral scales of snakes caused by nanoscale steps. *Bioinspir. Biomim.* **15**, 056014 (2020).
31. P. Vignaud *et al.*, Geology and palaeontology of the Upper Miocene Toros-Menalla hominid locality, Chad. *Nature* **418**, 152–155 (2002).
32. M. Schuster *et al.*, The age of the Sahara Desert. *Science* **311**, 821 (2006).
33. S. G. Wells, L. D. McFadden, J. C. Dohrenwend, Influence of Late Quaternary climatic changes on geomorphic and pedogenic processes on a desert piedmont, Eastern Mojave Desert, California. *Quat. Res.* **27**, 130–146 (1987).
34. M. Clarke, Infra-red stimulated luminescence ages from aeolian sand and alluvial fan deposits from the eastern Mojave Desert, California. *Quat. Sci. Rev.* **13**, 533–538 (1994).
35. H. Mendelssohn, On the biology of the venomous snakes of Israel II. *Isr. J. Zool.* **14**, 185–212 (1965).
36. C. Gans, H. Mendelssohn, "Sidewinding and jumping progression of vipers" in *Toxins of Animal and Plant Origin*, A. De Vries, E. Kochva, Eds. (Gordan and Breach, Science Publishers, Inc., New York, NY, 1971), pp. 17–38.
37. S. Spawls, B. Branch, *The Dangerous Snakes of Africa* (Ralph Curtis Books, Sanibel Island, FL, 1995).
38. T. M. Cover, *Elements of Information Theory* (John Wiley & Sons, Hoboken, NJ, 1999).
39. A. E. Filippov, S. N. Gorb, "Anisotropic friction in biological systems" in *Combined Discrete and Continual Approaches in Biological Modelling* (Biologically Inspired Systems, Springer, Cham, Switzerland, 2020), vol. 16, pp. 143–175.
40. S. S. Sharpe *et al.*, Locomotor benefits of being a slender and slick sand swimmer. *J. Exp. Biol.* **218**, 440–450 (2015).
41. R. D. Maladen, Y. Ding, C. Li, D. I. Goldman, Undulatory swimming in sand: Subsurface locomotion of the sandfish lizard. *Science* **325**, 314–318 (2009).
42. T. Zhang, D. I. Goldman, The effectiveness of resistive force theory in granular locomotion. *Phys. Fluids* **26**, 101308 (2014).
43. H. Askari, K. Kamrin, Intrusion rheology in grains and other flowable materials. *Nat. Mater.* **15**, 1274–1279 (2016).
44. P. E. Schiebel *et al.*, Mitigating memory effects during undulatory locomotion on hysteretic materials. *eLife* **9**, e51412 (2020).
45. J. M. Rieser *et al.*, Geometric phase and dimensionality reduction in locomoting living systems. arXiv [Preprint] (2019) https://arxiv.org/abs/1906.11374 (accessed 1 July 2020).
46. P. E. Schiebel *et al.*, Mechanical diffraction reveals the role of passive dynamics in a slithering snake. *Proc. Natl. Acad. Sci. U.S.A.* **116**, 4798–4803 (2019).
47. J. E. Baio *et al.*, Evidence of a molecular boundary lubricant at snakeskin surfaces. *J. R. Soc. Interface* **12**, 20150817 (2015).
48. M. C. G. Klein, S. N. Gorb, Ultrastructure and wear patterns of the ventral epidermis of four snake species (Squamata, Serpentes). *Zoology* **117**, 295–314 (2014).
49. S. Hirose, *Biologically Inspired Robots: Serpentile Locomotors and Manipulators* (Oxford University Press, Oxford, UK, 1993).
50. J. M. Rieser *et al.*, Snake microstructure. Open Science Framework. https://osf.io/kj9tv/. Deposited 17 November 2020.

EVOLUTION

BIOPHYSICS AND COMPUTATIONAL BIOLOGY

Rieser et al.
Functional consequences of convergently evolved microscopic skin features on snake locomotion

PNAS | 7 of 7
https://doi.org/10.1073/pnas.2018264118

www.manaraa.com